UV LEDs Based on *p-i-n* Core-Shell AlGaN/GaN Nanowire Heterostructures Grown by N-polar Selective Area Epitaxy*

Matt D. Brubaker[1], Kristen L. Genter[1,2], Alexana Roshko[1], Paul T. Blanchard[1], Bryan T. Spann[1], Todd E. Harvey[1], and Kris A. Bertness[1]

[1] Physical Measurement Laboratory, National Institute of Standards and Technology, Boulder, CO
[2] Department of Mechanical Engineering, University of Colorado, Boulder, CO

E-mail: matthew.brubaker@nist.gov

Received xxxxxx
Accepted for publication xxxxxx
Published xxxxxx

Abstract

Ultraviolet light-emitting diodes (UV LEDs) fabricated from N-polar AlGaN/GaN core-shell nanowires with *p-i-n* structure produced electroluminescence at 365 nm with ~5x higher intensities than similar GaN homojunction LEDs. The improved characteristics were attributed to localization of spontaneous recombination to the nanowire core, reduction of carrier overflow losses through the nanowire shell, and elimination of current shunting. Poisson-drift-diffusion modeling indicated that a shell Al mole fraction of x=0.1 in $Al_xGa_{1-x}N$ effectively confines electrons and injected holes to the GaN core region. AlGaN overcoat layers targeting this approximate Al mole fraction were found to possess a low-Al-content tip and high-Al-content shell, as determined by scanning transmission electron microscopy. Photoluminescence spectroscopy further revealed the actual Al mole fraction to be nanowire diameter dependent, where the tip and shell compositions converged towards the nominal flux ratio for large-diameter nanowires.

Keywords: GaN Nanowires, LEDs, AlGaN, N-polar, Core-shell, Selective Area Epitaxy

1. Introduction

Ultraviolet light-emitting diodes (UV LEDs) are used in an increasing number of applications related to spectroscopy, photopolymer curing, water purification, and medical disinfection [1]. Deep UV LEDs based on AlGaN nanowires (NWs) have received considerable attention recently [2-12], as the low quantum efficiencies typically encountered in high-Al-contant AlGaN can be mitigated by the high structural quality of self-assembled nanostructures. While planar LEDs emitting at near-UV wavelengths already possess relatively high external quantum efficiencies, NW-based devices can still provide new functionalities related to their discrete nature and nanoscale size. For example, single-NW UV LEDs could enable new tools for sub-diffraction optical lithography [13] that could be scaled up into pixelated arrays for wafer-level optical lithography.

To date, most published accounts of NW-based UV LEDs report on axial structures, grown either by random nucleation processes [2, 5, 6, 8-12, 14] or Ga-polar selective area epitaxy [7], or on randomly nucleated core-shell structures [15]. While core-shell LEDs based on selective area growth are widely reported for visible-wavelength emitters [16], relatively few reports exist on fully conformal core-shell UV LEDs [3]. However, NWs grown by N-polar selective area epitaxy [17] present several favorable attributes including high-aspect ratios for large LED active regions, arbitrarily large pitch spacings suitable for growth of single NWs with core-shell geometry, and integration with silicon substrates for potential integration with CMOS driver

circuitry. Furthermore, tailoring the strain state of the GaN core with the AlGaN shell composition and thickness could potentially enable polarization control [18] and wavelength tuning [19] of the emitted light.

In this work, we show that the use of a *p*-type AlGaN shell layer, intended to confine electrons to the *n*-type GaN core and be transmissive to radiating photons, increases the electroluminescence (EL) intensity by a factor of ~5 times and shifts the peak luminescence to 365 nm. Previously we have demonstrated core-shell N-polar GaN NW LEDs, which consisted of an *n*-type core conformally coated with a *p*-type Mg:GaN shell layer [3]. These LEDs produced EL at 380 nm that was attributed to donor-acceptor-pair (DAP) recombination resulting from electrons injected in the the *p*-type shell layer. We utilized 2D modeling to analyze spontaneous recombination in the core-shell LED structure and show reduced carrier overflow losses and enhanced carrier distribution with increasing Al mole fraction in the shell layer. The structure and composition of AlGaN/GaN core-shell heterostructures were characterized by analytical techniques and optical measurements were performed to provide additional insight on the diameter dependence of the AlGaN shell characteristics.

2. 2D modelling of core-shell NW LEDs

Recombination profiles and current flows were analyzed for a core-shell geometry by solving the coupled poisson and drift/diffusion equations using Next Nano ++ software [20]. Only spontaneous recombination processes were considered and strain effects were neglected in these 2D models. As shown in figure 1(a), the core-shell geometry comprised an *n*-type GaN core (300 nm diameter), an undoped *i*-AlGaN shell layer (85 nm thick), and a *p*-type AlGaN shell (285 nm thick), which roughly corresponds to the dimensions of the GaN-based *p*-*i*-*n* LED devices discussed in ref [3]. Shell layer thicknesses were increased at the NW tip to account for the higher growth rates in the axial direction. An acceptor concentration N_a=3x10^{19} cm^{-3}, hole mobility μ_h=10 cm^2/Vs, and activation energy of 200 meV was used for the *p*-type regions and a donor concentration N_d=5x10^{17} cm^{-3}, electron mobility μ_e=1000 cm^2/Vs, and activation energy of 15 meV was used for the *n*-type regions. The simulations were run under 3.3 V forward bias conditions, by use of *p*-contacts surrounding the entire *p*-AlGaN shell and an *n*-contact located at the base of the *n*-GaN core.

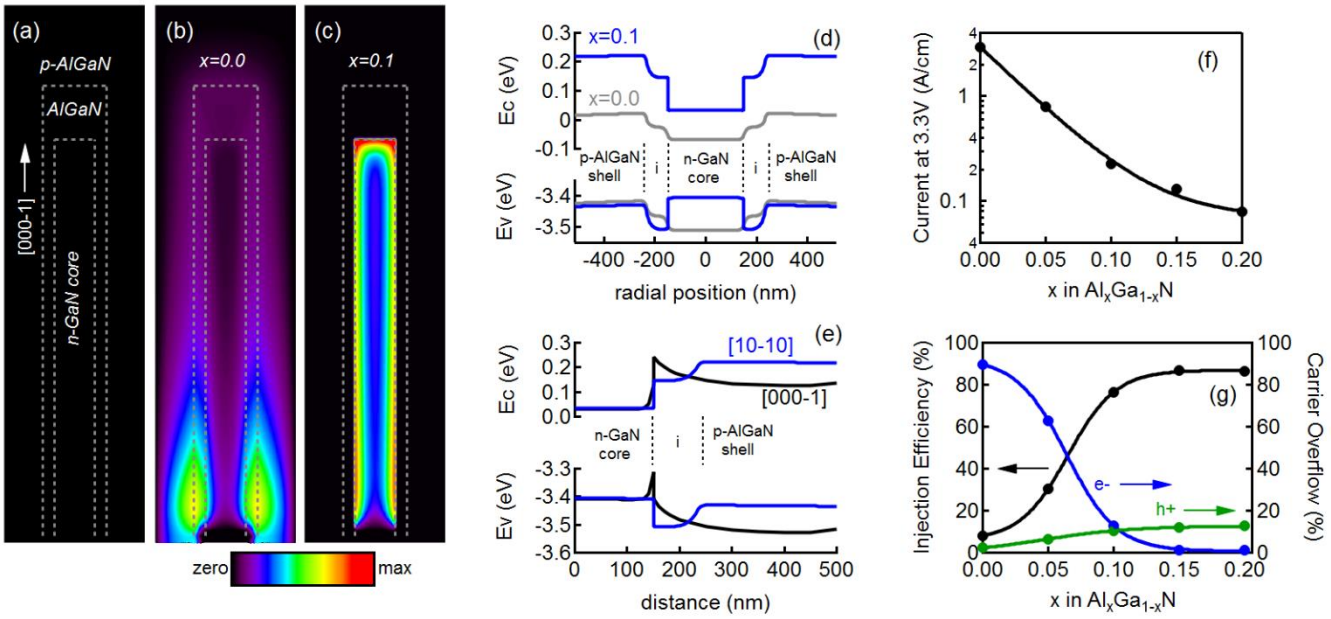

Figure 1. 2D models of core-shell AlGaN/GaN NW LEDs forward biased at 3.3 V and with varying Al mole fraction in the shell layer. The simulated structure is shown in (a) along with the resulting spontaneous recombination profiles for (b) x=0.0 and (c) x=0.1. Band diagrams comparing x=0.0 and x=0.1 in the radial direction are shown in (d) and band diagrams comparing the axial and radial directions for x=0.1 are shown in (e). The (f) simulated current integrated over the 2D contact surfaces at 3.3 V forward bias and (g) injection efficiency/carrier overflows are shown as a function of Al mole fraction.

It is readily apparent from figure 1(b,c) that the recombination profiles change dramatically with increasing Al mole fraction in the shell layer. For the GaN *p*-*i*-*n* homojunction (x=0.0), spontaneous recombination occurs primarily in the *p*-GaN shell layer, whereas recombination in the AlGaN/GaN *p*-*i*-*n* heterojunction (x=0.1) is restricted to the *n*-GaN core region. As shown

in the radial band diagrams ([10-10] direction) of figure 1(d), the GaN homojunction presents a symmetric barrier for injection of both electrons and holes, while electrons in the AlGaN/GaN heterojunction are confined to the core region by the large conduction band offset. Current flow in the heterojunction device is thereby limited to hole injection into the *n*-type core, the extent of which depends on the Al mole fraction and is shown for a fixed forward bias in figure 1(f).

The simulations also show that recombination is localized towards the nanowire base in the case of x=0.0, due to a shunt path of injected electrons that resembles current crowding effects discussed previously [21]. In contrast, recombination for the heterojunction device is more uniformly distributed along the entire core region and increases slightly towards the nanowire tip. This increase is related to polarization-induced band banding that results from the [000-1] N-polar orientation (figure 1(e)), creating a potential well in the valence band that confines injected carriers and lowers the barrier for hole injection. This effect appears to be unique to the N-polar orientation, as simulations performed in the [0001] Ga-polar direction do not exhibit the same increased recombination rate at the tip (not shown).

The confinement provided by the AlGaN/GaN heterojunction structures also reduces carrier overflow losses. The injection efficiency is the ratio of the total recombination rate in the active device region (which is defined here as the entire nanowire structure) divided by the carrier injection rate. As shown in figure 1(g), the injection efficiency increases from 8 % to 77 % by incorporating an AlGaN shell with an x=0.1 Al mole fraction. This approximate order-of-magnitude increase in the injection efficiency is directly related to the reduction in electron overflow at the *p*-contact. There is a slight increase in the hole overflow loss to the core contact, but this is relatively minor in comparison to the electron overflow and can be attributed to the long axial length relative to the shell thickness and the low hole mobility relative to the electron mobility.

3. **Synthesis and characterization of AlGaN/GaN core-shell heterostructures**

In this section, we focus on the synthesis and characterization of AlGaN/GaN nanowires grown by N-polar selective area epitaxy, approximately targeting the x=0.1 mole fraction shells that were theoretically shown to enhance LED performance in the previous section. It has been reported by others [22] that growth conditions exert a profound influence on axial and radial AlGaN growth rates. Alloy inhomogeneities between the NW tip and sidewall sections have also been reported for AlGaN shell layers, due to differences in surface-diffusion-induced transport of Ga and Al adatoms [23]. Here, we utilize analytical measurements to examine these effects for conditions specific to the growth of conformal *p*-type shell layers, which have previously been demonstrated in functional GaN *p-i-n* homojunction LEDs. We further examine the diameter dependence of the alloy inhomogeneities by use of photoluminescence (PL) spectroscopy on NW arrays with variable diameter and pitch spacing.

3.1 N-polar selective area epitaxy

Ordered NW arrays were grown by plasma assisted molecular beam epitaxy (PAMBE) using procedures and conditions discussed in detail elsewhere [3, 17]. In brief, the arrays in this study were grown on Si (111) substrates with N-polar GaN/AlN buffer layers. Silicon nitride growth mask layers were deposited and patterned by e-beam lithography to produce hole arrays with nominal diameters of 80 nm – 240 nm and pitch spacings of 300 nm – 10000 nm. Si-doped GaN cores were then grown at a substrate temperature of 860 °C (as measured by back-surface pyrometry [24]) and to a length of approximately 2 μm. The substrate temperature was lowered to 700 °C during a growth interruption, after which an Si-doped AlGaN shell was grown with group III fluxes and duration equivalent for growth of a 300 nm thick planar $Al_xGa_{1-x}N$ layer with x=0.09. A separate growth run with no AlGaN overcoat was used to correlate the actual GaN NW core diameters to the nominal hole sizes.

3.2 Analytical characterization

Scanning transmission electron microscopy (STEM) and energy dispersive X-ray spectroscopy (EDS) were used to assess the structural and compositional variations of NWs from an array with 160 nm nominal hole diameters and 1000 nm pitch. The TEM lamella were prepared by focused ion beam (FIB) milling for imaging along the <11-20> zone axis. As shown in figure 2, the high-angle annular dark field (HAADF) images show Z-contrast corresponding to the GaN core, a low-Al-content tip section, and a high-Al-content shell section. Also visible is contrast resulting from defects and thickness variations. The AlGaN tip length for the three NWs in figure 2(a) is ~440 nm and the AlGaN shell thickness is ~40 nm (averaged over the full length of leftmost NW), which translates into an approximate order of magnitude difference between the axial and radial growth rates. The contrast in the shell region on the left side of figure 2(b) probably resulted from a combination of the nonplanar side facets on the NWs (discussed below) and a slight misalignment of the FIB section through the NW. Thus, the contrast variations correspond to projections through regions of varying thickness, rather than to compositional variations in the shell. The uniform

shell contrast on the right side of figure 2(b) supports this possibility; however, top-down TEM imaging along the [0001] zone axis would be required to definitively answer this question.

EDS line scans along the length of the NWs were used to confirm the relative Al content of the tip and shell sections. It should be noted that these measurements have not been calibrated against samples with known Al alloy fractions and are reported here only for qualitative comparisons. As shown in figure 2(c), the Al content is near zero for the GaN core and is high/low for the shell/tip sections, respectively, which correlates well with the contrast in the HAADF images. EDS scans of the AlGaN tip exhibit large variation (both within and between scans) with respect to the HAADF contrast for the same region, which we consider to be measurement noise. Nonetheless, the EDS scans do appear to reproduce the inhomogeneous shell features that were noted above. EDS scans of the AlGaN shell (figure 2(d)) exhibit a uniform thickness along the NW length, indicating conformal AlGaN coating of the entire NW. The apparent non-zero Al content in the core section of figure 2(d) is an artifact due to a slight sample tilt during FIB preparation, which caused a portion of the shell behind or in front of the nanowire to be included in the cross section.

TEM images were also used to assess the relative crystal quality of the core and shell regions. Of the three NWs studied, the GaN cores were found to be nearly defect free, with the exceptions being a threading dislocation that bends towards the surface and annihilates near the NW base (not shown) and an inversion domain (ID, visible in figure 2(e)), which is generally considered to be a luminescent defect [25]. In contrast, the AlGaN tip sections were frequently observed to have stacking faults (SFs), which are likely a result of the lower substrate temperature used for AlGaN shell growth. As discussed in the modelling section above, recombination occurs in the GaN core for the AlGaN/GaN heterostructure LEDs, which is a favorable situation when considering the comparatively lower defect density of the N-polar GaN core regions observed in the TEM images.

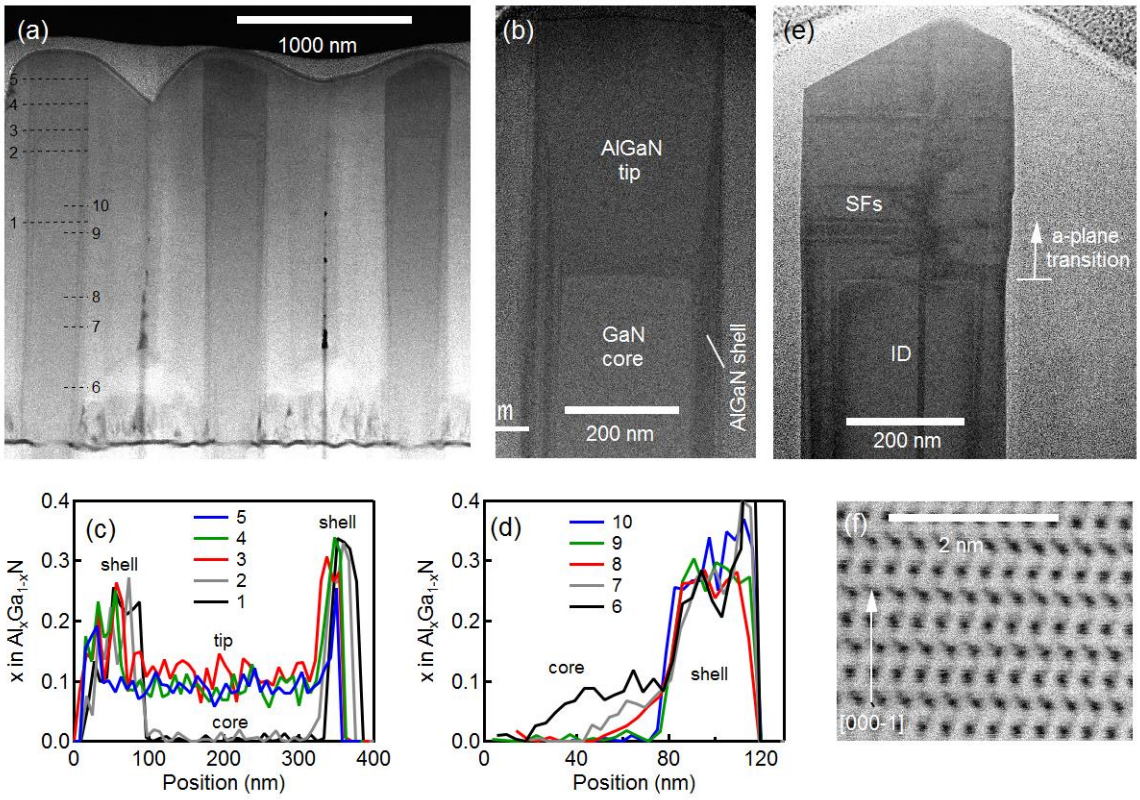

Figure 2. High-angle annular dark field (HAADF) TEM images of (a,b) AlGaN/GaN NWs with 160 nm nominal hole diameter and 1000 nm pitch spacing showing overall structure. EDS line scans are shown for the (c) NW tip and (d) NW sidewall sections, with scan positions indicated by the numbered lines in (a). Note that the mole fractions indicated in (c,d) have not been calibrated against known standards. A HAADF TEM image showing stacking faults (SFs) in the AlGaN shell and an inversion domain (ID) originating in the GaN core and penetrating the AlGaN shell are shown in (e). The transition from *m*- to *a*-plane faceting is also shown in (e) and found to coincide with the AlGaN/GaN interface at the NW tip. The atomic bright field (ABF) lattice image in (f) confirms the NW orientation to be N-polar orientation. All images were obtained for the <11-20> zone axis.

The NW sidewalls evolve from *m*- to *a*-plane surfaces during low-temperature shell growth, leading to a 30° rotation in the sidewall faceting. This transition is most apparent at the NW tip where both axial and radial growth occurs and results in an increased diameter, as indicated in figure 2(e). This feature provides a convenient marker for measuring the AlGaN tip length by SEM imaging and allows its overall length to be measured for a range of core diameters. As shown in figure 3(e), the length of the *a*-plane segment (which agrees with the TEM-based measurement of the AlGaN tip length) exhibits a clear dependence on the NW core diameter. The origin of this effect lies in the adsorption of fluxes incident on the NW sidewalls and diffusion-induced transport of surface adatoms that feed the high growth rate of the *c*-plane tip surface. As the adsorption rate on the NW sidewalls is proportional to diameter and incorporation rate at tip surface area is proportional to the diameter squared, the tip growth rate is inversely related to the NW diameter [26]. However, the surface diffusion length of Al adatoms has been identified to be significantly shorter than for Ga adatoms, leading to the high-Al-content shell (which experiences a net loss of Ga) and the low-Al-content tip (which experiences a net gain of Ga) [23].

Some NWs adopted a nanotripod or flower-like tip morphology (as shown in the upper right-hand corner of figure 3(c)) that became more prevalent in small-diameter NW arrays. These structures have been reported to nucleate on zincblende inclusions, which possess structural similarities to the stacking faults discussed above and form on the NW tip due to limited adatom mobility during low-temperature growth [27]. Considering that the diffusing Ga flux and associated high tip growth rate would be expected to produce higher stacking fault densities, it is likely that small-diameter NWs would be particularly susceptible to the formation of nanotripod structures.

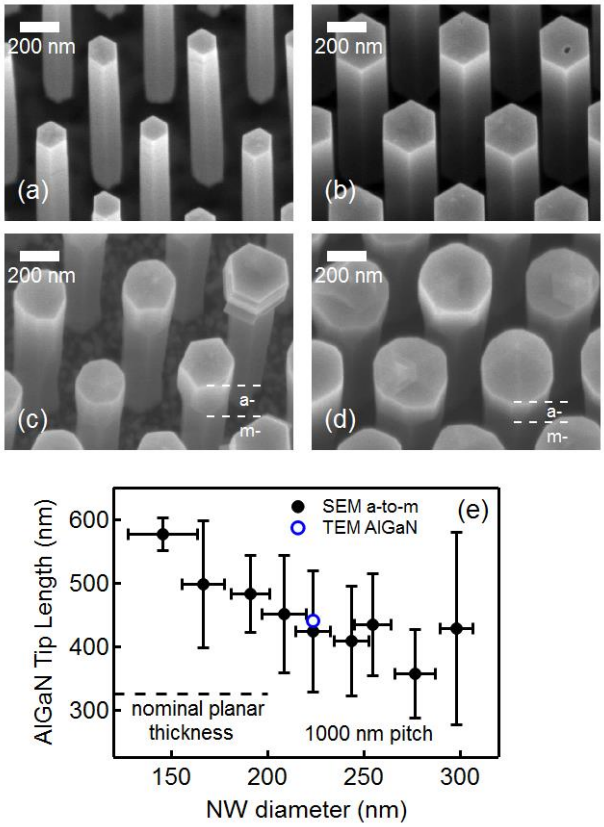

Figure 3. SEM images of GaN NW cores grown by selective area epitaxy on patterned substrates with nominal hole sizes of (a) 100 nm and (b) 200 nm diameter and pitch spacings of 500 nm. Images of AlGaN/GaN core-shell NWs corresponding to the same hole sizes in (a,b) are shown in (c,d), respectively. The overall length of the *a*-plane facets, indicated by the dashed lines in (c,d), are plotted against the measured core diameters in (e). The open circle in (e) is the AlGaN tip length measured by TEM and the dotted line indicates the equivalent planar thickness calculated from growth rates.

3.3 Optical characterization

The AlGaN/GaN NW arrays were further characterized by PL measurements to quantitatively determine the tip/shell alloy compositions as a function of NW diameter and pitch spacing. The spectra were obtained in a backscattering geometry using an excitation wavelength of 266 nm from a frequency-quadrupled Q-switched Nd:YVO_4 laser modulated at 15 kHz and with a

pulse duration of 8 ns [28]. Luminescence was dispersed by a scanning monochromator onto a photomultiplier tube detector and spectral intensities were measured by a lock-in amplifier locked to the modulation frequency of the laser. Time-resolved PL measurements were obtained using a frequency-tripled, mode-locked Ti:sapphire laser (266 nm) and time-corrleated single photon counting electronics [28]. Samples were mounted in the cryostat in their as-grown, on-chip configurations.

There are two primary features in the 5 K PL spectra, the higher energy of which corresponds to the AlGaN tip section (figures 4(a,b)). The peak energy positions were determined via gaussian peak fitting over a range of NW diameters and pitch spacings and are shown in figure 4(c). NW arrays with pitch spacing larger than 1000 nm were omitted from the figure, as luminescence from non-selective AlGaN growth on the mask layer becomes non-negligible with respect to the NW luminescence. A quantitative assessment of the Al mole fraction was then obtained from the composition-dependent bandgap: $E_g^{AlGaN} = E_g^{AlN}x + E_g^{GaN}(1-x) - bx(1-x)$, where x is the Al mole fraction, E_g^{AlN} (6.2 eV) and E_g^{GaN} (3.471 eV) are the AlN and GaN bandgaps, respectively, and b (1.0 eV) is the bowing parameter [29]. The tip composition was observed to vary by a few percent and trended toward lower Al mole fraction with decreasing NW diameter. As discussed above, small-diameter NWs incorporate a larger fraction of surface-diffusion-induced excess Ga, which dilutes the tip alloy concentration and shifts the luminescence towards lower energies (shown in figure 4(c)). The Al mole fraction was also found to become more concentrated with decreased NW pitch spacing. This was attributed to NW-to-NW shadowing effects in dense NW arrays that limit line-of-sight collection of beam fluxes (incident at 45° for our growth system). As discussed above, NW tip growth is fed by Ga surface diffusion from the NW sidewalls which dilutes the overall AlGaN composition. The sidewall collection area is limited to the NW tip segment for dense NW arrays, resulting in a reduced diffusion-induced gallium incorporation rate and a higher Al content in the tip segment. In contrast, large-pitch NW arrays will adsorb beam fluxes along the full NW length, resulting in increased diffusion-induced gallium incorporation rate and a lower Al content tip segment.

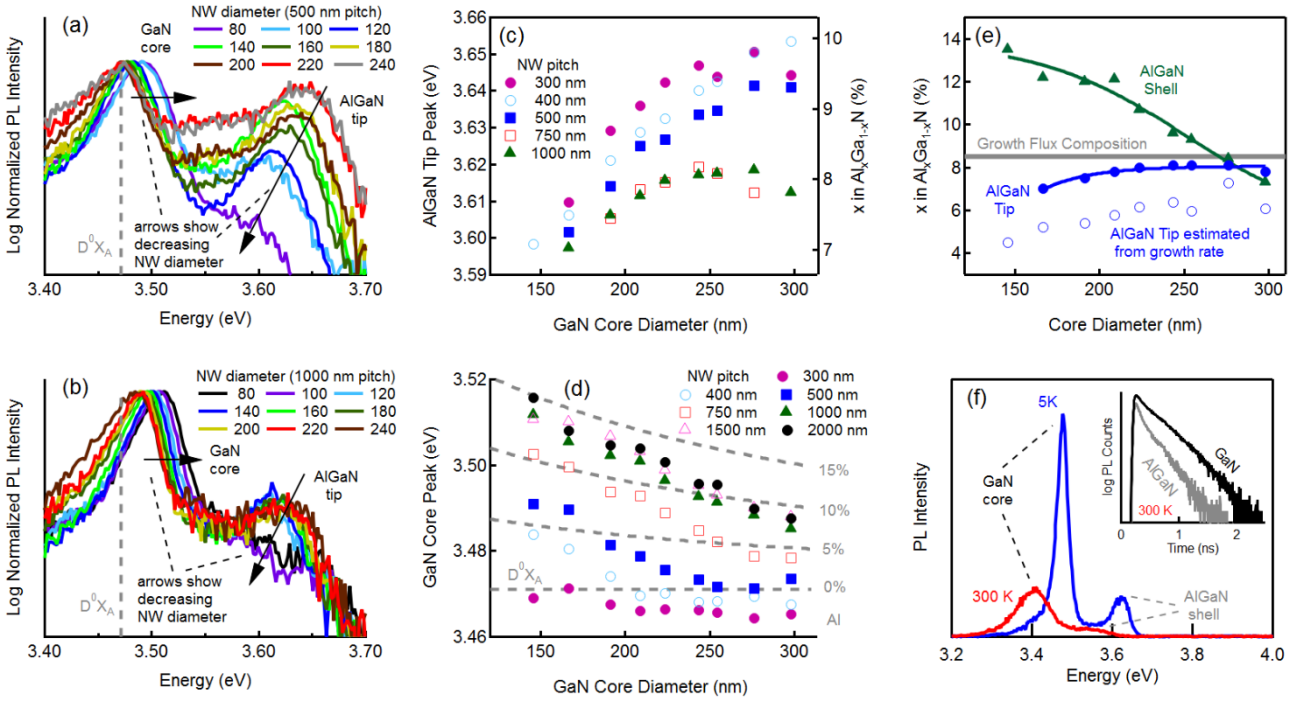

Figure 4. Diameter-dependent PL spectra of AlGaN/GaN core-shell NWs obtained at 5K for (a) 500 nm and (b) 1000 nm pitch spacings. Peak positions are shown for the (c) AlGaN tip and corresponding tip Al mole fraction calculated via bowing parameters and for the (d) GaN core along with calculated strain-induced shifts ($E_{A,B}$) for varying shell Al mole fraction (dashed lines). The overall tip/shell Al mole fractions determined by PL and by growth rate analysis are shown in (e) for NW arrays with 1000 nm pitch spacing. PL spectra obtained at 300 K and 5 K and time-resolved PL decay curves obtained at 300 K (inset) are shown in (f) for NWs from the 1000 nm pitch spacing and 160 nm nominal hole diameter array.

In principle, the AlGaN shell content could be determined directly from the emission energy; however, no NW-related luminescence was observed at the higher energies expected for high-Al-content shells. There are several possible scenarios that would account for this behavior, including non-radiative recombination due to a high density of defects or surface states

[30], surface-band-bending induced carrier transfer from the AlGaN shell prior to recombination, or in-plane emission due to re-ordering of valence sub-bands in high-Al-content AlGaN [18]. In lieu of directly measuring the AlGaN shell luminescence, we instead infer the shell composition from the strain that it exerts on the GaN core. For a given AlGaN shell thickness, the magnitude of the lattice mismatch strain and resulting shift in the core PL emission energy will depend on the shell composition. The compressive strain in the GaN core (ε_{zz}^{core}) is calculated as [31]:

$$\varepsilon_{zz}^{core} = \frac{F}{1+F} \cdot \frac{c_{AlGaN} - c_{GaN}}{c_{GaN}}, \qquad (1)$$

$$F = \frac{4\left(t_s^2 + D_{NW} t_s\right)}{D_{NW}^2} \cdot \frac{C_{33}^{AlGaN}}{C_{33}^{GaN}} \cdot \left(\frac{c_{GaN}}{c_{AlGaN}}\right)^2, \qquad (2)$$

where c_{AlGaN} and c_{GaN} are the *c*-direction lattice parameters of the shell and core, respectively, D_{NW} is the NW diameter, t_s is the shell thickness, and C_{33}^{AlGaN} and C_{33}^{GaN} are the elastic moduli of the shell and core, respectively. The compositional dependence of the AlGaN shell is implicitly represented in c_{AlGaN} and C_{33}^{AlGaN} using Vegard's law. The axial strain is related to the energy of the A,B ($E_{A,B}$) and C exciton transitions (E_C) through the deformation potentials [32]:

$$E_{A,B} = E_{A,B}(0) + (a_{cz} - D_1 - D_3) \cdot \varepsilon_{zz}^{core}, \qquad (3)$$

$$E_C = E_C(0) + (a_{cz} - D_1) \cdot \varepsilon_{zz}^{core}, \qquad (4)$$

where $a_{cz} - D_1$ and D_3 are the deformation potentials relevant to strain in the *c*-direction and are -4.9 eV and 8.2 eV, respectively [33]. The donor-bound exciton (D^0X_A) energy of 3.471 eV [34] was used for the strain-free A,B exciton transition energy ($E_{A,B}(0)$) and 3.50 eV was used for the strain-free C exciton transition energy ($E_C(0)$) [32]. The calculated values of $E_{A,B}$ for various Al mole fractions (using the TEM-measured shell thickness of 40 nm) are shown as dashed lines in figure 4(d) along with the experimentally measured peak positions of the strained GaN core. We note that $E_{A,B} < E_C$ for the NW diameters and AlGaN shell thickness and composition used in this part of the study, thus only the A,B exciton transition is considered in the following discussion. For arrays with large pitch spacings (1000 nm - 2000 nm), where uniform AlGaN shells are obtained and self-shadowing effects can be neglected, the experimental peak positions show an Al content of ~7 % for large-diameter NWs that increases to ~14 % for smaller-diameter NWs. The excess Ga incorporated at the NW tip represents a net loss for sidewall incorporation and effectively increases the Al mole fraction of the AlGaN shell. This trend becomes less evident for small pitch spacings and is likely due to the non-uniform shell layer, which might induce photogenerated carrier transport to and recombination in the strain-free NW sections.

The diameter-dependent Al mole fraction is summarized for both tip and shell sections in figure 4(e). The Al composition of the incident flux (~9 %) is also plotted in the figure. Arrays with 1000 nm pitch spacing were chosen for this comparison as an optimized trade-off in maximizing shell uniformity and minimizing non-selective growth between the NWs. Both the shell and tip compositions are approximately equal to that of the incident flux for large diameter NWs. However, the tip and shell compositions diverge with decreasing NW diameter according to redistribution of Ga adatoms by surface diffusion. In fact, the smallest nanowires possess a shell content approximately twice that of the tip. As a comparative estimate, the tip alloy fraction was calculated directly from the fluxes using the excess tip growth rates shown in figure 3(e) as a diameter-dependent first-order correction. These estimates are shown by the open circles in figure 4(e) and reproduce the overall trend of the PL-derived data.

The relative PL intensities and overall optical quality of the GaN core and AlGaN tip sections were assessed at room temperature, which are more representative of LED operational conditions. As shown in figure 4(f), the 300 K PL intensity of the AlGaN shell is substantially reduced over that of the GaN core and is possibly related to the higher defect densities observed during TEM imaging (e.g. stacking faults in figure 2(e)). Stacking fault densities were also speculated in the previous section to increase in proportion to the AlGaN tip growth rate (in explanation of the higher fraction of nanotripod defects observed small-diameter NW arrays) and might also account for the PL intensity reduction for small diameter NWs shown in figures 4(a,b). Time-resolved photoluminescence (TRPL) measurements performed at 300 K further indicate that the PL lifetime of the AlGaN shell (τ~0.12 ns) was approximately half that of the GaN core (τ ~0.25 ns), as shown in the inset of figure 4(f). This indicates that the non-radiative recombination rate is higher for the AlGaN shell and is likely attributed to the unpassivated AlGaN surface or the aforementioned defects. In contrast, the GaN cores are passivated by the AlGaN shell and have a higher structural quality as shown by the TEM images in figure 2. These results suggest that NW LEDs based on the AlGaN/GaN core-shell structure would possess a higher internal quantum efficiency (in addition to the enhanced carrier injection efficiency discussed previously), as carrier recombination is isolated from the nanowire surfaces.

4. **N-polar AlGaN-GaN core-shell p-i-n NW LEDs**

Core-shell NW LEDs were grown using GaN core and AlGaN shell growth conditions similar to those described above, but with modifications to the doping schedule and overall duration in order to produce a *p-i-n* LED structure similar to the GaN

homojunction LEDs discussed in reference [3]. *N*-type GaN NW cores were first grown to an estimated length of 3.3 μm and with a pitch spacing of 5 μm (which completely avoids shadowing effects). A growth interruption was applied for the transition to shell growth conditions, after which the surface was refreshed with a ~15 nm thick *n*-type GaN layer. The AlGaN shell was then grown in three segments: an ~85 nm thick undoped *i*-layer, followed by a ~285 nm thick Mg-doped *p*-layer, and finally a ~5 nm thick heavily-doped *p*+ layer to minimize *p*-contact resistance. The thicker AlGaN shell layers used here produced NW diameters that are considerably thicker than those used for PL test structures (figure 5(a)). As such, it is likely that the alloy composition of the tip and shell sections converged towards the nominal flux ratio of x=0.09. A two-stage metallization was used for *p*-contacts and consisted of an initial Ni (20nm)/Au (200 nm) layer deposited at normal incidence and a second 200 nm Au layer was deposited at 45° (with no rotation). This provides electrical contact to one side of the NW, while leaving the other side unmetallized for light extraction. Contact was made to the *n*-type cores through the GaN buffer layer, using the silicon nitride growth mask layer to provide electrical isolation from the overlying *p*-contact layer [3].

The electrical characteristics were measured for AlGaN/GaN NW LEDs (x~0.09) and were compared against the GaN homojunction LEDs (x=0.0) discussed in reference [3]. As shown in figure 5(b), both LED types produce diode-like current-voltage (I-V) characteristics with turn-on voltages near the GaN bandgap and low reverse bias leakage currents. The AlGaN/GaN LEDs exhibited a higher turn-on voltage and/or series resistance than the GaN LEDs, which is likely related to the reduced electron overflow current (figure 1(g)) and increased barrier to hole injection (figure 1(d)) expected for higher Al mole fractions. We also note that the device characteristics of the AlGaN/GaN LEDs improve with prolonged forward bias current injection, which resulted in increased EL intensities and decreased series resistance. Similar improvements in LED characteristics have been reported elsewhere and were attributed to electrical annealing [35]. As no post-contact anneal was utilized in the AlGaN/GaN LEDs (for comparability to the GaN LED devices), we tentatively attribute the improved characteristics to electrical annealing of the *p*-contact during operation. For the present study, all devices were run under constant current conditions until the EL intensity and forward bias stabilized. However, further development of optimized *p*-contact metallization and annealing processes are expected to reduce burn-in effects and improve overall device performance.

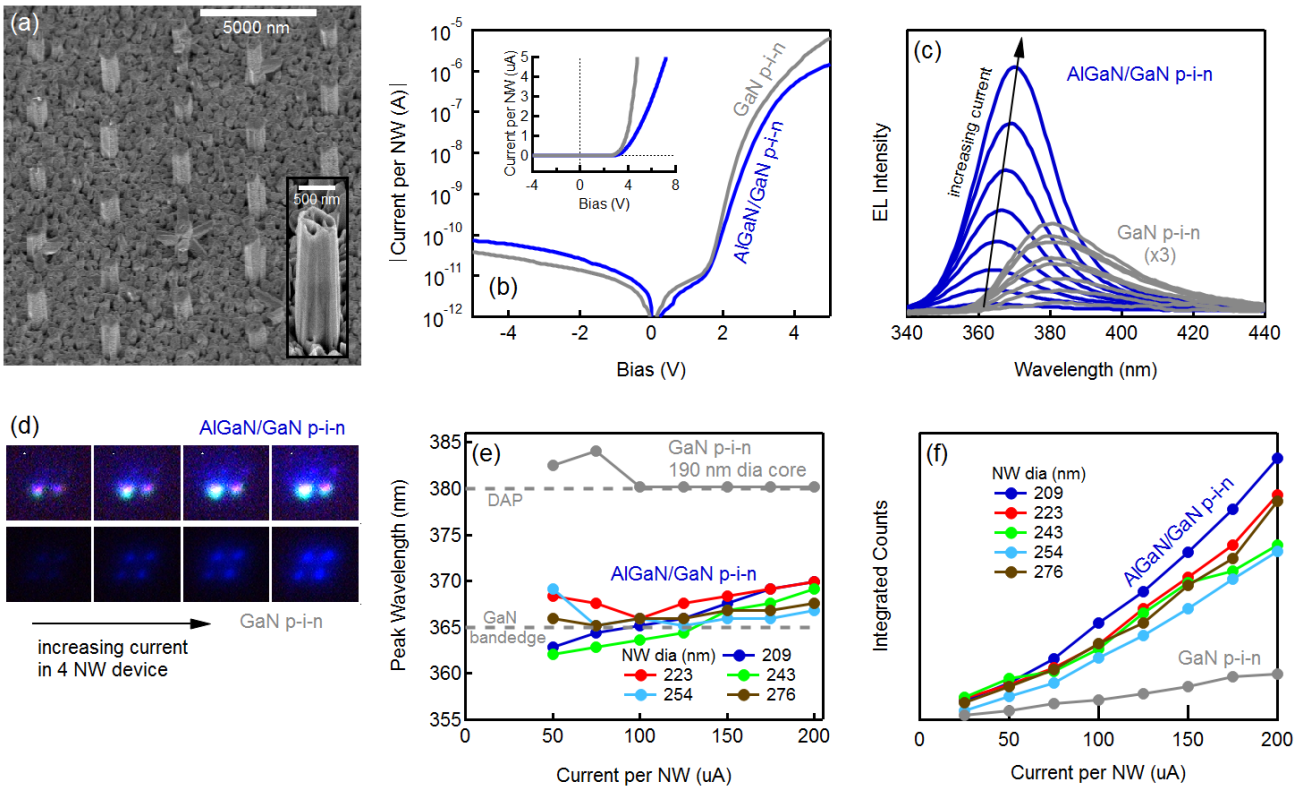

Figure 5. Core-shell *p-i-n* NW LED characteristics comparing device structures based on AlGaN/GaN heterojunctions and GaN homojunctions. SEM images of a post-metallization AlGaN/GaN core-shell LED structure with 25 NWs is shown in (a), with the inset showing the pre-metallization single NW morphology. The (b) I-V characteristics and (c) EL spectra for 25 NW LED devices and (d) EL images for 4 NW LED devices are shown in the figure. For clarity, the GaN *p-i-n* EL intensities have been multiplied by a factor of three (x3). The (e) peak emission wavelength and (f) integrated intensity vs current are also shown for various GaN core diameters.

As shown in figure 5(c,e), the AlGaN/GaN LEDs produced electroluminescence (EL) at a wavelength corresponding to the GaN band-edge (365 nm), while the GaN LEDs emitted at a wavelength corresponding to donor-acceptor-pair recombination (380 nm). Donor-acceptor-pair emission results from recombination in heavily doped *p*-type GaN and indicates that EL in the GaN homojunction devices is due to electrons injected in the the *p*-type shell layer and/or that EL emanating from the core is reabsorbed by the shell. In contrast, the 365 nm EL for AlGaN/GaN LEDs is indicative of recombination of injected holes in the *n*-type GaN core region (rather than recombination in the higher bandgap AlGaN shell). These experimental determinations localize the source of EL emission, which map well to the simulated 2D recombination profiles shown in figures 1(b,c). Furthermore, the AlGaN/GaN LEDs also exhibited ~5x higher integrated intensities than the GaN LEDs at a given current injection level (figure 5(f)), which reflects the increased injection efficiency predicted by the simulations (figure 1(g)).

The AlGaN/GaN LEDs exhibit a spectral redshift with increasing current injection that is not observed in the GaN LEDs. In fact, a small blueshift was observed at low current levels in the GaN LEDs that was attributed to screening of potential fluctations or filling of Mg-related states during DAP recombination in the *p*-type shell [3], similar to excitation-intensity-dependent PL spectral blueshifts reported elsewhere [34]. For the AlGaN/GaN LEDs, it is likely that the spectral characteristics are dominated by temperature-dependent Varshi effects that produce spectral redshifts as a result of device self-heating. It is expected that this effect was active in the GaN LEDs as well, but was compensated by the current-injection-based blueshift for DAP recombination.

No consistent trends in the overall spectral characteristics were observed as a function of NW core diameter (in the range of ~210-275 nm); however, individual NWs within the arrays exhibited intensity variations as shown in figure 5(d). The simulation results shown in figure 1f suggest that current injection at a given forward voltage would be sensitive to compositional fluctuations, such as those identified during STEM imaging (Fig 2). These compositional variations might account for some of the NW-to-NW dispersion in optical output shown in figure 5(d). Structural inhomogenieties related to nanotripod formation, porous tip surfaces, or the non-uniform metallization may also influence light extraction and contribute to non-uniform emission.

5. **Conclusions**

AlGaN/GaN core-shell nanowire heterostructures grown via N-polar selective area epitaxy were fabricated into UV LEDs and demonstrated to produce EL intensities ~5x higher than similar GaN homojunction LEDs. These core-shell stuctures effectively confined carrier recombination to the high-quality GaN core, resulting in electroluminescence at the GaN bandgap energy and an overall reduction in the carrier overflow losses. In contrast, homojunction LEDs produced electroluminescence through donor-acceptor-pair transitions in the more defective Mg:GaN shell layer and further suffered from high carrier overflow losses, current shunting near the NW base, and optical re-absorption in the shell. Modeling indicated that a shell Al mole fraction of x~0.1 was sufficient for obtaining the majority of beneficial carrier confinement effects, including a uniform spontaneous recombination profile that efficienctly utilized the enhanced junction area of the core-shell nanowire LED. Array-based PL and STEM EDS measurements further indicated the that actual AlGaN shells comprised low-Al-content tip and high-Al-content shell segments with a diameter-dependent composition resulting from surface-diffusion-induced transport of Ga adatoms from the sidewalls to the tip during growth. While the structures investigated here targeted the approximate composition required for carrier confinement, higher Al mole fractions may present additional opportunities for future work in strain-engineering of the GaN core for wavelength tuning and polarization/emission control. These fully conformal AlGaN/GaN core-shell heterostructures (which are not widely reported in the literature) were made possible by N-polar selective area epitaxy techniques, which enables growth of essentially isolated NW cores that are not subject to line-of-sight considerations during subsequent AlGaN shell growth.

Acknowledgements

This is a contribution of an agency of the US government and is not subject to copyright.

References

[1] Kneissl M *et al.* 2011 Advances in group III-nitride-based deep UV light-emitting diode technology *Semicond Sci Tech* **26** 014036
[2] Carnevale S D, Kent T F, Phillips P J, Mills M J, Rajan S and Myers R C 2012 Polarization-Induced pn Diodes in Wide-Band-Gap Nanowires with Ultraviolet Electroluminescence *Nano Lett* **12** 915-20
[3] Brubaker M D, Genter K L, Weber J C, Spann B T, Roshko A, Blanchard P T, Harvey T E and Bertness K A 2018 Core-shell p-i-n GaN nanowire LEDs by N-polar selective area growth *SPIE Nanoscience + Engineering* **10725** 1072502-1

[4] Coulon P M, Kusch G, Martin R W and Shields P A 2018 Deep UV Emission from Highly Ordered AIGaN/AIN Core-Shell Nanorods *Acs Appl Mater Inter* **10** 33441-9
[5] Janjua B *et al.* 2017 Droop-free AlxGa1-xN/AlyGa1-yN quantum-disks-in-nanowires ultraviolet LED emitting at 337 nm on metal/silicon substrates *Opt Express* **25** 1381-90
[6] Kent T F, Carnevale S D, Sarwar A T M, Phillips P J, Klie R F and Myers R C 2014 Deep ultraviolet emitting polarization induced nanowire light emitting diodes with AlxGa1-xN active regions *Nanotechnology* **25** 455201
[7] Liu X H, Le B H, Woo S Y, Zhao S R, Pofelski A, Botton G A and Mi Z T 2017 Selective area epitaxy of AlGaN nanowire arrays across nearly the entire compositional range for deep ultraviolet photonics *Opt Express* **25** 30494-502
[8] Mi Z *et al.* 2016 Molecular beam epitaxial growth and characterization of Al(Ga)N nanowire deep ultraviolet light emitting diodes and lasers *J Phys D Appl Phys* **49** 364006
[9] Zhao S *et al.* 2015 Aluminum nitride nanowire light emitting diodes: Breaking the fundamental bottleneck of deep ultraviolet light sources *Sci Rep-Uk* **5**
[10] Zhao S, Woo S Y, Bugnet M, Liu X, Kang J, Botton G K and Mi Z 2015 Three-Dimensional Quantum Confinement of Charge Carriers in Self-Organized AlGaN Nanowires: A Viable Route to Electrically Injected Deep Ultraviolet Lasers *Nano Lett* **15** 7801-7
[11] Zhao S *et al.* 2016 Molecular beam epitaxy growth of Al-rich AlGaN nanowires for deep ultraviolet optoelectronics *Apl Mater* **4**
[12] Zhao S R and Mi Z T 2018 AlGaN Nanowires: Path to Electrically Injected Semiconductor Deep Ultraviolet Lasers *Ieee J Quantum Elect* **54**
[13] Naber A, Kock H and Fuchs H 1996 High-resolution lithography with near-field optical microscopy *Scanning* **18** 567-71
[14] Brubaker M D *et al.* 2013 Toward Discrete Axial p-n Junction Nanowire Light-Emitting Diodes Grown by Plasma-Assisted Molecular Beam Epitaxy *Journal of electronic materials* **42** 868-74
[15] Ra Y H, Kang S and Lee C R 2018 Ultraviolet Light-Emitting Diode Using Nonpolar AlGaN Core-Shell Nanowire Heterostructures *Adv Opt Mater* **6** 1701391
[16] Li S F 2014 *Wide Band Gap Semiconductor Nanowires 2*, ed V Consonni and G Feuillet (London, UK, Hoboken, NJ: ISTE;John Wiley & Sons, Inc.) pp 135-59
[17] Brubaker M D, Duff S M, Harvey T E, Blanchard P T, Roshko A, Sanders A W, Sanford N A and Bertness K A 2016 Polarity-Controlled GaN/AlN Nucleation Layers for Selective-Area Growth of GaN Nanowire Arrays on Si(111) Substrates by Molecular Beam Epitaxy *Cryst Growth Des* **16** 596-604
[18] Jacopin G *et al.* 2012 Photoluminescence polarization in strained GaN/AlGaN core/shell nanowires *Nanotechnology* **23** 325701
[19] Hetzl M, Kraut M, Winnerl J, Francaviglia L, Doblinger M, Matich S, Morral A F I and Stutzmann M 2016 Strain-Induced Band Gap Engineering in Selectively Grown GaN-(Al,Ga)N Core-Shell Nanowire Heterostructures *Nano Lett* **16** 7098-106
[20] Certain commercial equipment, instruments or materials are identified to adequately specify the experimental procedure. Such identification does not imply recommendation or endorsement by the National Institute of Standards and Technology, nor does it imply that the materials or equipment identified are necessarily the best available for the purpose.
[21] Connors B, Povolotskyi M, Hicks R and Klein B 2010 Simulation and design of core-shell GaN nanowire LEDs *SPIE OPTO* **7597** 11
[22] Carnevale S D, Yang J, Phillips P J, Mills M J and Myers R C 2011 Three-Dimensional GaN/AIN Nanowire Heterostructures by Separating Nucleation and Growth Processes *Nano Lett* **11** 866-71
[23] Allah R F, Ben T, Songmuang R and Gonzalez D 2012 Imaging and Analysis by Transmission Electron Microscopy of the Spontaneous Formation of Al-Rich Shell Structure in AlxGa1-xN/GaN Nanowires *Appl Phys Express* **5** 045002-1
[24] Bertness K A, Brubaker M D, Harvey T E, Duff S M, Sanders A W and Sanford N A 2014 In situ temperature measurements for selective epitaxy of GaN nanowires *Physica Status Solidi C: Current Topics in Solid State Physics, Vol 11, No 3-4* **11** 590-3
[25] Auzelle T, Haas B, Den Hertog M, Rouviere J L, Daudin B and Gayral B 2015 Attribution of the 3.45 eV GaN nanowires luminescence to inversion domain boundaries *Appl Phys Lett* **107** 051904
[26] Debnath R K, Meijers R, Richter T, Stoica T, Calarco R and Luth H 2007 Mechanism of molecular beam epitaxy growth of GaN nanowires on Si(111) *Appl Phys Lett* **90** 123117
[27] Wang P *et al.* 2017 Lattice-Symmetry-Driven Epitaxy of Hierarchical GaN Nanotripods *Adv Funct Mater* **27** 1604854
[28] Schlager J B, Sanford N A, Bertness K A and Roshko A 2011 Injection-level-dependent internal quantum efficiency and lasing in low-defect GaN nanowires *J Appl Phys* **109** 044312
[29] Yun F, Reshchikov M A, He L, King T, Morkoc H, Novak S W and Wei L C 2002 Energy band bowing parameter in AlxGa1-xN alloys *J Appl Phys* **92** 4837-9
[30] Reszka A *et al.* 2016 An influence of the local strain on cathodoluminescence of GaN/AlxGa1-xN nanowire structures *J Appl Phys* **120** 194304
[31] Hestroffer K *et al.* 2010 The structural properties of GaN/AlN core-shell nanocolumn heterostructures *Nanotechnology* **21** 415702
[32] Rigutti L, Jacopin G, Largeau L, Galopin E, Bugallo A D, Julien F H, Harmand J C, Glas F and Tchernycheva M 2011 Correlation of optical and structural properties of GaN/AlN core-shell nanowires *Phys Rev B* **83** 155320
[33] Vurgaftman I and Meyer J R 2003 Band parameters for nitrogen-containing semiconductors *J Appl Phys* **94** 3675-96
[34] Reshchikov M A and Morkoc H 2005 Luminescence properties of defects in GaN *J Appl Phys* **97** 5623
[35] Zhao C *et al.* 2016 Droop-Free, Reliable, and High-Power InGaN/GaN Nanowire Light Emitting Diodes for Monolithic Metal-Optoelectronics *Nano Lett* **16** 4616-23